Research Article | Vol. 29, No. 5 / 1 March 2021 / Optics Express 7261

Optics EXPRESS

Toward high laser power beam manipulation with nanophotonic materials: evaluating thin film damage performance

T. U. TUMKUR,[1] R. SOKHOYAN,[2] M. P. SU,[2] A. CEBALLOS-SANCHEZ,[1] G. KAFAIE SHIRMANESH,[2] Y. KIM,[2] H. A. ATWATER,[2] E. FEIGENBAUM,[1,4] AND S. ELHADJ[1,3,5]

[1]*National Ignition Facility and Photon Science, Lawrence Livermore National Laboratory, Livermore, CA 94550, USA*
[2]*Thomas J. Watson Laboratory of Applied Physics, California Institute of Technology, Pasadena, CA 91125, USA*
[3]*Currently at: Seurat Technologies, Inc.,265 Ballardvale St, Wilmington, MA 01887, USA*
[4]*feigenbaum1@llnl.gov*
[5]*selhadj@seuratech.com*

Abstract: Nanophotonic materials enable unprecedented control of light-matter interactions, including the ability to dynamically steer or shape wavefronts. Consequently, nanophotonic systems such as metasurfaces have been touted as promising candidates for free-space optical communications, directed energy and additive manufacturing, which currently rely on slow mechanical scanners or electro-optical components for beam steering and shaping. However, such applications necessitate the ability to support high laser irradiances (> kW/cm^2) and systematic studies on the high-power laser damage performance of nanophotonic materials and designs are sparse. Here, we experimentally investigate the pulsed laser-induced damage performance (at $\lambda \sim$ 1 μm) of model nanophotonic thin films including gold, indium tin oxide, and refractory materials such as titanium nitride and titanium oxynitride. We also model the spatio-thermal dissipation dynamics upon single-pulse illumination by anchoring experimental laser damage thresholds. Our findings show that gold exhibits the best laser damage resistance, but we argue that alternative materials such as transparent conducting oxides could be optimized to balance the tradeoff between damage resistance and optical tunability, which is critical for the design of thermally robust nanophotonic systems. We also discuss damage mitigation and ruggedization strategies for future device-scale studies and applications requiring high power beam manipulation.

1. Introduction

Engineered nanophotonic optical components in the form of photonic crystals, plasmonic devices, and metamaterials have unfurled counterintuitive physical phenomena and enabled unparalleled applications ranging from sensing to energy harvesting, photocatalysis and quantum information processing [1–3]. Conventionally, the optical response of nanophotonic components cannot be modified after fabrication. However, a number of active nanophotonic devices such as integrated photonic circuits, spatial light modulators (SLMs) [4] and metasurfaces [2,5,6] enable post-fabrication tunability. These active nanophotonic devices enable dynamic control of light via application of external stimuli, which can be electrical or optical, for example. These advances in dynamic light manipulation have enabled fast and efficient beam steering [7], thermal emission control [8] and adaptive optical elements [6,9].

A significant number of current and prospective applications of nanophotonic materials require the ability to handle high laser irradiances, repetition rates and optical fluences. Such applications include advanced lithography, adaptive optics, directed energy, state-of-the-art laser systems

#413843 https://doi.org/10.1364/OE.413843
Journal © 2021 Received 2 Nov 2020; revised 13 Feb 2021; accepted 15 Feb 2021; published 23 Feb 2021

Optics EXPRESS

and laser-based manufacturing [10,11]. As an example, metal additive manufacturing (AM) typically employs continuous wave (CW) process lasers (at $\lambda \sim 1$ μm) with high powers (up to kW), required to selectively melt metallic powder [12]. However, metal AM techniques rely on bulky optics to handle high irradiances (~ kW/cm^2) and mechanical galvanometric scanners to steer the process laser beam to build parts layer-by-layer, which limits the speed (to ~ kHz) that can affect control over microstructure and mechanical properties of printed components [12]. SLMs based on digital micromirror devices (DMDs) or microelectromechanical systems offer an alternative route by enabling dynamic beam steering, but suffer from poor laser power handling capabilities, limited to tens of W/cm^2, well below levels needed to drive the thermal processes necessary for AM [4]. Alternatively, liquid crystals (LC)-based SLM technologies such as optically addressable light valves [12,13] allow for beam steering with relatively higher damage thresholds and power handling capability. However, efficient operation in such devices typically necessitates increasing thickness of the LC layer, leading to bulky form factors and rapid degradation of modulation speeds [13]. Nanophotonic devices can potentially bridge the tradeoffs between functionality efficiency and laser damage resistance but their practical and fundamental optical power handling limits remain unknown. Prior research has shown that active metasurfaces can perform all-solid-state dynamic beam steering and beam shaping [5,14–16] without employing mechanically moving parts. Active metasurfaces, which are actively tunable arrays of subwavelength optical elements, may exhibit high modulation frequencies (above MHz speeds) with reduced device complexity [6,7,17]. Their ultrathin form also makes them suitable for high laser power applications in principle since the accumulated heat can be dissipated more efficiently. The rationale behind illustrating metal AM as a target application is to highlight the fact that the irradiances (few kW/cm^2 as an upper bound) and switching speeds (kHz – MHz) necessitated by AM applications are indeed tangible by incorporating clever damage mitigation and nanophotonic device engineering strategies, as will be discussed here. Acquiring such know-how would also propel efforts towards making more robust devices for applications requiring higher operational irradiances (such as directed energy and adaptive optics for laser systems).

However, achieving superior optical and laser damage performance of metasurfaces (and nanophotonic devices in general) is nontrivial, requiring a thorough consideration of optical, electrical, and thermal properties of the constituent materials. Achieving dynamic functionality further increases device complexity, with the need to integrate an actively tunable material into the metasurface structure [5,17]. For instance, prior efforts have reported electrically tunable beam steering metasurfaces consisting of metallic layers (necessary to elicit plasmonic response and conductivity), a tunable "active" material with dynamically controllable optical properties, and a capping film, all with different optoelectronic and thermal responses. Metals are generally not tunable (unless ultrathin metallic films are considered [18]), and large inherent carrier concentrations are thought to lead to strong optical losses [19]. In an effort to mitigate losses, several strategies have explored improving fabrication and compensating losses with gain media. Additionally, greater tunability for functionality in the visible and NIR, has been achieved using alternative materials such as strongly doped semiconductors and refractory ceramics such as titanium nitride (TiN) [19–22]. Transparent conducting oxides (TCOs) such as indium tin oxide (ITO) have also been widely utilized as transparent alternatives to metallic contacts, and as active materials [22–25]. Additionally, intermediary phases of alternative plasmonic materials such as titanium oxynitrides (TiN_xO_y) [26,27], as well as phase change materials such as vanadium dioxide VO_2 [28,29], GSTs [30,31], have also been proposed as actively tunable layers, which can be integrated into otherwise passive nanophotonic structures. However, optimizing nanophotonic device efficiency and functionality still necessitates the use of multiple functional elements rather than monolithic architectures.

Optics EXPRESS

The presence of multiple layers of different materials introduces thermomechanical stresses that can reduce damage resistance in comparison to a single thin film layer or monolithic structures [11,32]. Furthermore, the presence of subwavelength optical elements in the form of nanoantennas or thin metal-dielectric multilayers leads to starkly different thermal dissipation dynamics in comparison to bulk, homogeneous structures. The strong field localization in nanophotonic structures can also result in larger optical losses and at high laser powers, the propensity for laser damage increases further, since sub-wavelength inclusions and interfaces generate large amounts of heat, leading to irreversible damage [32–34]. Added to the complication, the laser damage performance of nanophotonic devices such as metasurfaces and their constituent materials such as structured metals, TCOs, or alternative plasmonic materials, has not been studied well, or is simply unknown. Although the laser damage properties of traditional optical components such as thin dielectric coatings, mirrors and gratings have been studied since the inception of lasers, laser damage mechanisms (even in conventional materials) depend on several intrinsic and extrinsic factors including the laser pulse duration, wavelength and repetition rate [32,35,36]. Hence, design considerations for high laser power operation using nanophotonic devices, are largely driven by the target application space. For instance, directed energy applications require higher power vis-NIR CW (or longer than ns pulse) irradiance (> tens of kW) [37],where the performance of current mechanical beam steering optics is largely limited by thermal damage mechanisms. On the other hand, applications such as parallel two-photon lithography-based AM require femtosecond (fs) laser irradiance to deliver high peak fluences at $\lambda = 800$ nm, but operation lifetimes and pulse cycles are bound by the non-thermal damage mechanisms of beam steering DMDs [38,39]. As a proposed target, if ~1 kW over 1 cm^2 aperture of CW laser intensity handling is possible, while maintaining tunable optical properties at NIR wavelengths, it would enable un-equaled AM technologies based on laser beam steering metasurfaces. Hence, designing functional nanophotonic devices for specific high-power laser applications behooves a thorough understanding of laser-induced damage mechanisms in connection to the optical performance of constituent materials.

To this end, a few studies have investigated wide bandgap semiconductors [33], thin metallic films and TCOs such as ITO and aluminum doped zinc oxide (AZO) [34,40]. Diamond was also reported to have good CW laser damage resistance for use as a highly reflective surface at NIR wavelengths due to its high thermal conductivity [11]. Nanostructured TiN was shown to exhibit robust laser damage resistance, superior to gold nanostructures, but for ultrafast (fs) irradiation [41,42]. Subsequent ultrafast studies of refractory materials using transient reflectivity measurements indicated stronger electron-phonon coupling compared to Au [43]. However, there has not been a comprehensive study of laser damage performance focused on the optical and electrical properties of optical thin film components, in the context of applicability to realistic nanophotonic devices.

Here, we systematically evaluate the pulsed (ns) laser damage performance - in the regime where heating remains a key failure mode - and extract the optical and electrical properties of a broad range of thin film materials, which can be used in functional nanophotonic devices such as metasurfaces. The thin films studied here include Au, ITO and varying stoichiometries of titanium nitride-based compounds ($Ti_{1-x-y}N_xO_y$) whose optical properties were tuned to exhibit metallic, epsilon-near-zero (ENZ) and dielectric behavior in the visible to NIR regimes [26,27]. We perform these experiments at a wavelength of $\lambda = 1.06$ μm – the spectral region of interest for a wide range of applications including metal AM. We then perform thermal modeling, anchored by experimentally acquired laser damage threshold fluences, and model the dynamics of temperature distribution in the thin films studied experimentally.

Optics EXPRESS

2. Methods

Thin film fabrication: Thin films of Au, ITO, titanium nitride (TiN) and titanium oxynitride (TiN_xO_y) were deposited onto double sided polish sapphire substrates for laser damage studies, and on 2" silicon wafers for optical characterization (ellipsometry). A 50 nm thin Au film was also deposited on a fused silica substrate for comparison. TiN and TiN_xO_y films were grown at room temperature via reactive high-power impulse magnetron sputtering of a 2-inch diameter Ti target, in either an Ar/N_2 atmosphere for TiN, or an $Ar/N_2/O_2$ atmosphere for TiN_xO_y. After loading the substrates, the vacuum chamber was pumped down over night until reaching a base pressure of 4×10^{-5} Pa. The operating pressure was 0.4 Pa with a total gas flow of 20 sccm and an Ar/N_2 gas flow ratio of 17/3 sccm for TiN. For TiN_xO_y, the total gas flow was increased to 30 sccm to achieve plasma stability, and it consisted of a fixed 25 sccm Ar and variable N_2/O_2 ratios to tune the composition of the films. A Starfire Industries power supply sourced 550 W pulses to the Ti target at a frequency of 1000 Hz and duration of 50 µs. The substrate was negatively biased with a constant DC voltage of 200 V. Growth rates varied from 0.05 - 0.15 nm/s. The ITO film was deposited using room-temperature RF magnetron sputtering from an ITO target. Argon (Ar) gas with a flow rate of 20 sccm was used to strike the plasma, while a mixture of Ar and oxygen (O_2) (Ar/O_2:90/10) with a flow rate of 0.6 sccm was injected to control the amount of oxygen deficiency, and hence, the charge carrier concentration of the ITO layer. The deposition pressure and the applied RF power were set to 3 mTorr and 48 W, respectively. Using the mentioned deposition parameters, the deposition rate of ITO was obtained to be about 1.1 nm/minute. The Au film was deposited via electron beam evaporation with a deposition rate of 1 Å/s.

Laser damage studies: Single-shot laser damage experiments were performed using a pulsed Nd:YAG laser at the fundamental wavelength $\lambda = 1064$ nm. The laser pulses carried Gaussian temporal profiles (with FWHM pulse duration $\tau = 3.6 \pm 0.5$ ns) and were incident normal to the sample plane and focused, generating a Gaussian beam spot with diameter (at $1/e^2$) ~165 µm. The pulse energy was controlled using a thin-film polarizer and a half-wave plate and the fluence was varied between ~ 0.05 J/cm^2 – 9 J/cm^2. Ex-situ confocal microscopy (Keyence VR-3000 and Keyence VK-X100) was used to obtain optical images of damaged spots for further analysis post laser exposure. The laser damage performance can be visualized by plotting the area of each damage site as a function of input fluence on a semi-log scale, followed by linearly fitting the data points (Fig. 2). The intersection of the extrapolated linear fit through abscissa yields the threshold fluence (F_{th}), or the laser-induced damage threshold (LIDT), above which irreversible damage occurs [32,34]. Any observable modification upon laser irradiation, including change in contrast, cracking, or the appearance of surface roughness, was considered damage. All the experimental damage studies were limited to single shot damage irradiance.

Optical and electrical characterization: The optical constants of the films and sapphire substrates were extracted by performing spectroscopic ellipsometry measurements (J. A. Woollam) at incident angles of 65°, 70° and 75°. The optical constants of Si substrates were obtained from the J. A. Woollam WVASE software database. The complex dielectric permittivity (given as $\varepsilon = \varepsilon' + i\varepsilon''$) was extracted by fitting the ellipsometric data to a Drude-Lorentz model. The model consists of one Drude term and up to three Lorentz oscillators (in order account for the interband contributions) and is given as [44,45]:

$$\varepsilon(\omega) = \varepsilon_\infty - \frac{\omega_p^2}{\omega^2 - i\Gamma_D\omega} + \sum_{j=1}^{n} \frac{f_j\omega_{0j}^2}{\omega_{0j}^2 - \omega^2 + i\gamma_j\omega} \quad (1)$$

Here, ε_∞ is the background permittivity due to bound electrons, ω_p is the plasma frequency (with energy $E_p = \hbar\omega_p$), Γ_D is the Drude damping factor. From the Lorentz terms in the equation, ω_{0j} is the oscillator position (with energy $E_{0j} = \hbar\omega_{0j}$), f_j is the oscillator strength and γ_j is the Lorentz broadening. The values of fitting parameters, including the thicknesses of the films,

Optics EXPRESS

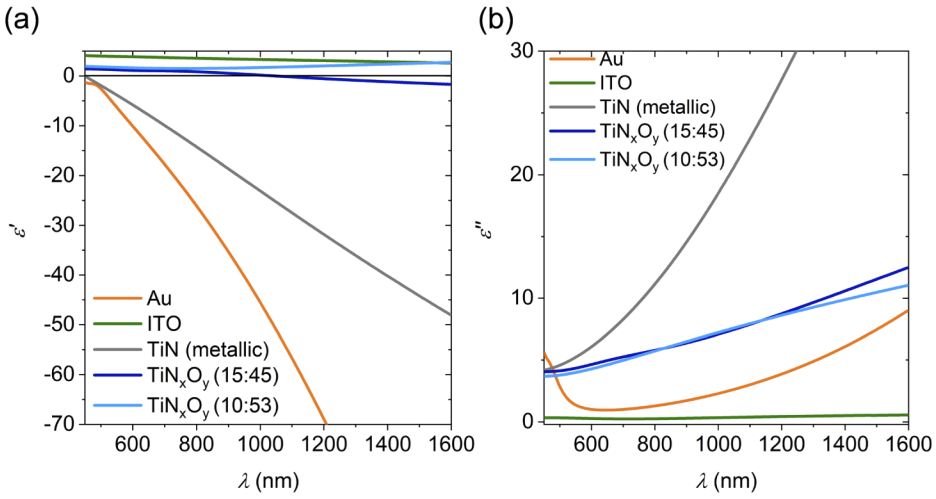

Fig. 1. The (a) real and (b) imaginary parts of the dielectric permittivity spectra for Au, ITO, TiN and titanium oxynitride thin films with two different stoichiometries (defined as the ratio N_2:O_2).

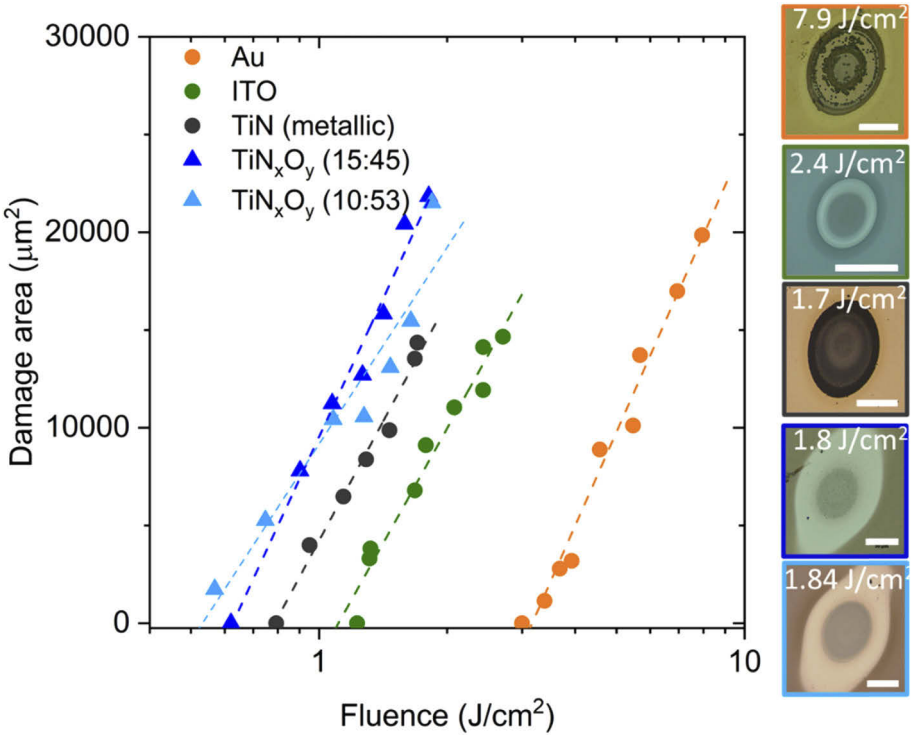

Fig. 2. Areas of damage sites produced by single pulse illumination, plotted as a function of varying input fluences. The dashed lines indicate linear fits to the data. Right panel – representative confocal microscopy images of the damaged spots (color-coded corresponding to respective films indicated in the left panel) at fluences higher than their respective F_{th} values, as indicated. Scale bars are 50 μm.

Optics EXPRESS

and the mean squared error (MSE) from fitting are given in Supplement 1, Table S1. Electrical transport properties (charge carrier concentration, mobility and resistivity) were also extracted from ellipsometric fit parameters, as described in the text. The electrical properties of gold and ITO films were also validated using DC Hall effect measurements.

Thermal modeling: As a first step, we investigate the laser damage of thin material films - 70 nm thick TiN, 50 nm-thick Au, and 50 nm thick ITO. When performing thermal analysis, we first calculate absorption density in each film, when the films were illuminated by a plane wave, using a transfer matrix formalism and using tabulated data for optical constants of individual layers [46]. Our simulations were performed by using discontinuous Galerkin time-domain (DGTD) algorithm implemented in the commercial package (Lumerical Inc). In our optical simulations, the absorption density is calculated at a wavelength of 1064 nm. As a next step, we incorporate the results of our optical simulations into a heat simulation package (Lumerical Inc). The temperature at the bottom of substrates is fixed to 300 K (the structure is coupled to a thermal bath). We have also assumed that the top of the considered structure is cooled via convection (ambient at 300 K). We performed both steady state and transient heat simulations, along with simulations under the device switching conditions. In our transient heat simulations, the full width at half maximum (FWHM) of the illuminating laser pulse was 3.6 ns ±0.5 ns, which corresponds to the pulse width measured and used in experiments. The thickness of the fused silica substrate is 500 µm while the thickness of the sapphire substrate is 446 µm. These substrate thickness values also correspond to substrate thicknesses used in the experiment. The thermal properties of ITO were taken from Ref. [47] and thermal properties of TiN were taken from the following materials database: (https://thermtest.com/materials-database#Titanium-nitride). In our simulations, we used thermoelectric properties of Au reported in Ref. [48]. For the thermoelectric properties of fused silica and Al_2O_3, we used the values from the Lumerical database. We expect that for experimental parameters for which the laser damage has been observed, the calculated maximal temperature in the films should be close to the melting temperature of the materials taken as the single pulse or single exposure damage criteria [33].

3. Experimental results

The dielectric permittivity spectra of all the samples reported in this work were extracted using spectroscopic ellipsometry, as detailed in the methods section and Supplement 1. Figure 1 shows the extracted complex dielectric permittivity spectra of a representative selection of thin film samples. For the sake of brevity, we mostly limit our discussions to five sample - Au, ITO, TiN_xO_y (47:5), TiN_xO_y (15:45) and TiN_xO_y (10:53), where the ratios indicate the relative elemental compositions (as %) of nitrogen and oxygen in the compound ($Ti_{1-x-y}N_xO_y$). Henceforth, we refer to TiN_xO_y (47:5) as 'TiN (metallic)', since the real part of its dielectric permittivity exhibits increasing negative values beyond the epsilon-near-zero (ENZ) point which occurs in the near-visible region, akin to other reports of metallic behavior in TiN [22,26]. A decrease in the x:y ratio in $Ti_{1-x-y}N_xO_y$ leads to reduced metallic behavior as evident from the real permittivity spectra of the two titanium oxynitride samples (TiN_xO_y (15:45) and TiN_xO_y (10:53)), Fig. 1. The ENZ transition wavelength for TiN_xO_y (15:45) is red-shifted in comparison to TiN (metallic) and the sample exhibits only a slightly metallic behavior (low magnitude of the real permittivity) in the NIR region of interest (1064 nm). TiN_xO_y (10:53) on the other hand does not exhibit ENZ transition in this wavelength range and behaves as a lossy dielectric material, where the magnitude of the imaginary part of permittivity remains higher than that of Au across most of the visible and NIR regions. The tunability of the optical properties of - TiN_xO_y, can be understood as a combination of TiN and TiO_2 phases, and the optical behavior is dependent on whether the compound is metal-rich (leading to more metallic behavior) or oxygen-rich, resulting in more dielectric behavior [26,27]. For our studies, the three sub-stoichiometric compositions in TiN represent a distinct set of refractory ceramic plasmonic platforms, whose optical properties

Optics EXPRESS

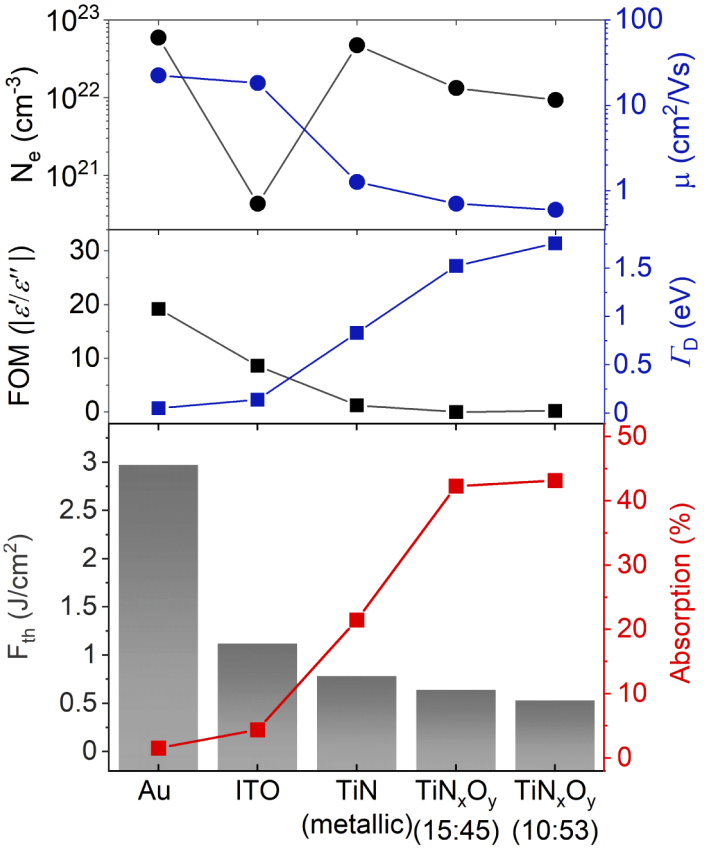

Fig. 3. Bottom panel - laser-induced threshold fluences extracted from single-pulse irradiation at $\lambda = 1064$ nm, on the thin films. Middle panel – optical figures of merit (FOM, black squares) and the Drude damping factor (Γ_D, blue squares) corresponding to the thin film samples, extracted using ellipsometry at $\lambda = 1064$ nm. Top panel – Charge carrier concentration (N_e, black circles) and mobility of charge carriers (μ, blue circles). The calculated absorption within each thin film layer is shown in the bottom panel, plotted on top of their respective threshold fluence values.

are tunable from metallic, to ENZ and dielectric behavior (Fig. 1). From Fig. 1, Au appears to have the best "metallic" performance across the NIR region of the spectrum, with lower losses and higher (most negative) magnitude of the real part permittivity. ITO, is a wide-bandgap semiconductor, classified as a transparent conductive oxide, whose carrier concentration can be tuned by heavy doping [23,25,40]. In our studies, ITO exhibits a low plasma frequency and behaves as a dielectric in the wavelength region of interest.

To relate the optical properties described above to the laser damage properties in the thin film samples, we measured the LIDT, Fig. 2. The laser-induced damage performance was evaluated by irradiating the sample with a single ns pulse with increasing laser fluences at different spots on the sample. Representative confocal microscope images of the damage sites acquired at moderately high fluence values (above F_{th}) are shown in the right panel of Fig. 2. It is important to note here that we consider any observable modification of the film at the irradiated spot as damage, including discoloration, increased surface roughness or cracking induced by thermomechanical stresses, and ablation induced by bulk melting. Several mechanisms ranging from thermal degradation (for CW beams), ablation dominated by absorption, to dielectric

Optics EXPRESS

breakdown and multiphoton ionization (for ultrashort pulses), could lead to damage, depending on the pulse width, repetition rate, thin film morphology, thickness and composition. However, the mode of damage in all the materials in our study, was dominated by bulk-heating induced by absorption, rather than defect-dominated absorption [32,35,40]. This is evident from the shape of the damaged spots, which closely track the Gaussian shape of the incident laser beam, at fluences both close to (Supplement 1, Fig. S2), and much higher than F_{th} (Fig. 2). We further substantiate the claim that damage is due to the excess thermal energy (from light absorption), which raises the thin film temperature close to its melting point (at the onset of damage), using optothermal simulations and calculated absorptions (Fig. 3), as described in subsequent sections. The morphologies of laser-induced damaged spots exhibit discoloration in the center at low fluences (and at the periphery for higher fluences), roughness, delamination or instability-driven cavitation at fluences past the thin film melting temperature (as for the Au film, Fig. 2), all of which are characteristics of bulk absorption-dominated damage [32,49].

The laser damage properties of a material are closely linked to its optical and electrical properties. For plasmonic thin films, the large carrier densities necessary to achieve metal-like behavior results in highly localized absorption and strong damping, which can lead to starkly different thermal behavior, depending on the film stoichiometry, or in comparison to conventional dielectric coatings or bulk materials. To address the interplay between laser damage resistance and optoelectrical properties, we model the total absorption within each thin film on a sapphire (with index n = 1.75) substrate. We also evaluate the optical figure of merit (FOM), which is expressed as $|\varepsilon'/\varepsilon''|$, by extracting the optical constants using spectroscopic ellipsometry measurements and fitting to a model consisting of one Drude and up to three Lorentz oscillator terms, as described in the methods section (Supplement 1,Fig. S1) . The model was chosen to effectively incorporate the free electron contribution (via the Drude term) and interband transitions (described by the Lorentz oscillators), to the overall optical response [44,45]. The optoelectronic response of plasmonic thin films in the vis-NIR can be understood well by the free electron contribution, which is characterized by the plasma frequency (ω_p) and the Drude damping factor (Γ_D). Hence, the charge carrier concentration (N_e) and mobility (μ) were extracted by ellipsometric fitting, as N_e depends on the plasma frequency as $\omega_p = \sqrt{\frac{N_e e^2}{\varepsilon_o m^*}}$ (where ε_o is the vacuum permittivity and e and m^* are the electron charge and effective mass, respectively). Additionally, Γ_D is related to the electron relaxation time (τ) as $\Gamma_D = \hbar/\tau$ (where $\tau = \mu m^*/e$). The complete set of parameters used to fit ellipsometry data are reported in the Supplement 1 (Table S1). The thin film resistivity values obtained using ellipsometry were in qualitatively good agreement with DC Hall measurements, although thin films with low mobilities exhibited unrealistically large values of charge carrier concentration in Hall measurements (data for Au and ITO shown in the Supplement 1, Fig. S2).

Figure 3 shows the calculated total absorption values, along with the experimentally extracted FOM, Γ_D, N_e and μ for each thin film sample at $\lambda = 1064$ nm, plotted alongside their respective LIDT(F_{th}) values. The LIDT values were measured with standard deviation error < 10% in both metallic and dielectric samples. Among the thin film samples considered here, Au exhibits the highest damage threshold, followed by ITO, TiN and the two titanium oxynitride samples. The laser damage resistance increases with decreasing absorption, which is unsurprising since the mode of damage in all thin films is predominantly dominated by bulk absorption, explained earlier. The absorption in materials is dictated by the imaginary permittivity component, which explains both the inverse scaling of the FOM with absorption and the anti-correlated threshold fluence (Fig. 3). The FOM is very high in Au since the magnitude of the real part of the permittivity is generally high at NIR wavelengths. Depending on the composition, the titanium oxynitride films behave either as a poor metal with ε' close to zero (TiN_xO_y (15:45)), or a lossy dielectric (TiN_xO_y (10:53)) with positive ε', but the FOMs are low for both the oxynitride films, since the FOM is dominated by the stronger contribution from ε''. While TiN exhibits metal-like

Optics EXPRESS

behavior (Fig. 1), it exhibits the strongest optical losses across most of the visible and NIR regions, among the thin films examined. Its FOM remains over an order of magnitude lower than that of Au throughout the NIR window examined here (Supplement 1). Although our TiN films are sub-stoichiometric, even "highly plasmonic" TiN films fabricated epitaxially exhibit optical FOMs that are significantly smaller than Au [22,50–52]. The optical response (and consequently the laser damage performance) of the thin films can be understood by electrical transport properties, which can be described by N_e and μ. It has previously been reported that laser damage mechanism exhibits a sharp transition from a defect-dominated to bulk absorption-dominated damage at $N_e > 10^{19}$ cm^{-3} for thin films [34]. In our studies, all the thin films possess large N_e values ($> 10^{20}$ cm^{-3}) as shown in Fig. 3, which further substantiates our claim that the mechanism of damage in the films is due to bulk absorption. Among the films studied here, Au exhibits the most "metallic" behavior, with the highest N_e and μ. The large inherent free carrier densities ($\sim 10^{23}$ cm^{-3}) in noble metals such as Au, results in large and negative ε'. The TiN (metallic) film also exhibits high N_e, comparable to Au, but the mobility of charge carriers in TiN is $\sim 17\times$ smaller than Au. This is significant because absorption (and damage) is directly related to $1/\mu$, and thus lower μ for a given N_e will produce a lowering of the damage threshold. The titanium oxynitride films exhibit four to five-fold smaller N_e ($\sim 10^{22}$ cm^{-3}) in comparison to Au, which in principle, should lead to reduced optical losses in comparison. However, μ also exhibits a two-fold decrease in the oxynitride films in comparison to TiN (metallic) and over a thirty-fold reduction compared to Au. ITO on the other hand, exhibits a relatively higher damage threshold and μ, despite its large carrier concentration. Although the optical and electrical properties of ITO can vary significantly depending on the processing conditions (for example, N_e can vary by $\sim$ two orders of magnitude), the measured N_e and μ values of our ITO films compare reasonably well with reported values of ITO films of similar thicknesses sputtered at room temperature [23,25,40,53,54]. The reduced mobility in nonstoichiometric TiN and oxynitride films arises from the large Drude damping (Γ_D) that occurs due to the metallic lattice being substituted by non-metallic inclusions. In general, the Drude damping factor (Γ_D) accounts for optical losses that arise due to electron-electron scattering, electron-phonon scattering and impurity and grain boundary scattering [55,56]. Note that an increase in the Γ_D results in poorer laser damage resistance since absorption-dominated thermal damage due to ns (or shorter) pulses, involves the heating of the lattice by charge carriers. Hence, Γ_D is a good metric to predict laser damage performance dominated by thermal dissipation, as evident by the good inverse correlation between LIDT and Γ_D. It is important to note that interband losses also affect the optical and thermal performance of thin films, which is not accounted for in any of the Drude parameters, but is taken into consideration in the Drude-Lorentz modeling used to extract the optical constants.

4. Transient heat simulations

Next, we model the temperature rise expected in the experimentally studied thin films, which occurs upon single pulse illumination [Fig. 4(a)]. For performing the thermal analysis, we employ a design flow that is commonly used in literature [57]. First, we calculate the absorption per unit volume (absorption density) within each thin film, using experimentally derived dielectric permittivity values at $\lambda = 1064$ nm (Fig. 1). The absorption density h is calculated according to $h(\mathrm{r}) = \frac{1}{2}\omega\varepsilon_0 \mathrm{Im}(\varepsilon)|\mathrm{E}(\mathrm{r})|^2$, where ω is the angular frequency of the incoming laser light, ε is the complex dielectric permittivity of the considered film, and E(r) is the complex amplitude of the electric field. The calculated absorption density is then fed into a thermal simulation package (https://www.lumerical.com/products/heat/) to calculate the spatial distribution of temperature as a function of time, upon the illumination by a single laser pulse with a FWHM of 3.6 ns. While the experimentally used laser pulse is Gaussian-shaped, in our simulations, we approximate the Gaussian pulse with a trapezoidal one [Fig. 4(b)] because of limitations of the used software package. In our heat simulations, we assume that the ambient temperature is 300 K, and that the

Optics EXPRESS

temperature at the bottom of the substrate is fixed to 300 K [Fig. 4(a)]. We also assume that the top surface of the film is cooled via natural convection with a convective heat transfer coefficient of 10 W/(m^{2}K).

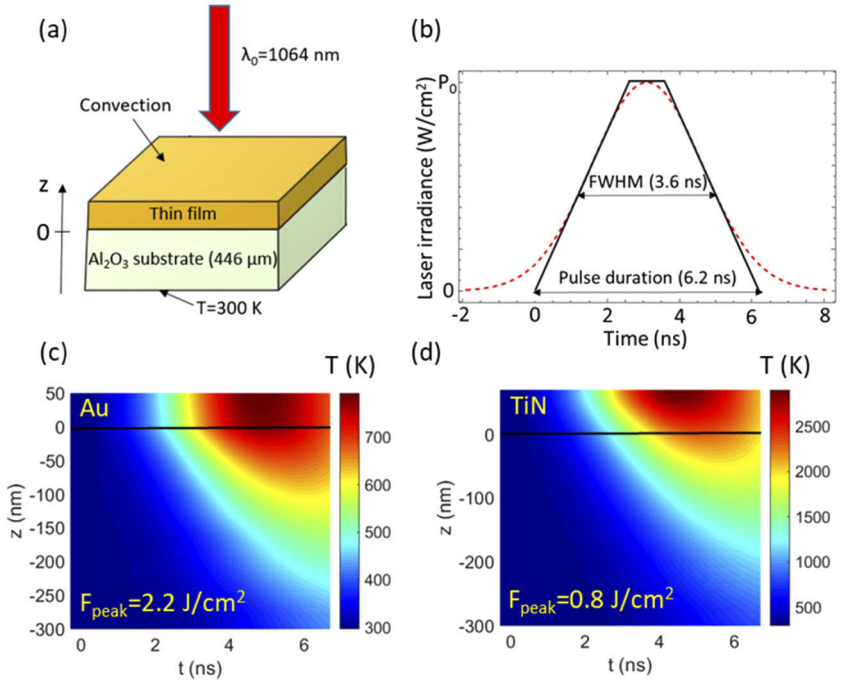

Fig. 4. (a) Schematic of a thin film placed on a sapphire substrate. (b) Laser irradiance as a function of time. In our simulations, the Gaussian temporal beam profile (dashed line) is approximated by a trapezoidal function (solid line). Temperature of the structure consisting of a thin film on a sapphire substrate as a function of time (t) and spatial (z) coordinate for (c) a 50 nm-thick Au film and (d) 70 nm-thick TiN (metallic) film on a sapphire substrate. The peak fluence (F_{peak}), wavelength (λ) and pulse duration FWHM (τ_{FWHM}) are input parameters in the model, obtained from experiments. The peak pulse power P_0 is calculated as F_{peak}/τ_{FWHM}. The horizontal line at z = 0 nm represents the interface between the substrate and the respective thin film considered in the study.

Figures 4(c) and 4(d) show the results of the thermal simulations for two representative thin film structures considered in the study –a 50 nm-thick Au film and a 70 nm-thick TiN (metallic) film on 446 μm-thick sapphire substrates with thermal conductivities of 28 W/(m×K). More specifically, Figs. 4(c) and 4(d) plot the temperature in the considered structures as a function of time and the z-coordinate. In Supplement 1, Fig. S3 shows the transient heat analysis on the remaining thin films considered in our studies. The peak fluence values (F_{peak}) considered in our simulations were equal to the threshold fluence (F_{th}) values that were extracted experimentally. As expected, the maximal temperature is observed at the interface of the considered film and the air due to higher absorption density in this region of the film. Thus, for an incident peak laser fluence of F_{peak} = 2.2 J/cm^2, the Au thin film reaches a maximum temperature ~ 793 K over the total pulse duration (6.2 ns), Fig. 4(a). For comparison, the melting temperature of bulk gold is 1337 K [44,58]. Similarly, the transient temperature map for the TiN (metallic) film, evaluated at $F_{peak} = F_{th}$ = 0.8 J/cm^2, is shown in Fig. 4(b). The maximum temperature reached over the same incident pulse duration is ~ 2900 K, much higher than that of Au. The melting temperature of TiN 3203 K [44].

Optics EXPRESS

Several notable observations can be made from the transient thermal dissipation simulations. Firstly, the maximal temperature rise in Au is significantly lower than in TiN – a direct consequence of the smaller absorbance (~1.5%) in comparison to TiN (~ 20%), as shown in Fig. 3. Although the melting point of TiN is higher than that of Au owing to its refractory nature, the combination of high doping density and relatively lower mobility results in greater absorption and reduced LIDT. A similar correlation between absorption and temperature rise can be seen in the titanium oxynitride and ITO thin films (Supplement 1, Fig. S3). We also note that the maximal calculated temperature rise in Au and TiN (metallic) are smaller than their respective melting temperatures. Although this may seem surprising, it is important to note that the threshold fluences extracted experimentally corresponded to the onset of *any* visible signs of damage, including discoloration, cracking, and ripple formation. While complete melting (at fluences beyond the melting threshold fluence) results in the flow and onset of removal of the film due to ablation or vaporization, discoloration is a result of surface oxidation that is known to occur at fluences below the melting threshold [32,49,59]. Similarly, cracking and ripple formation could result from thermomechanical stresses close to, but below melting temperatures [49]. On the other hand, transport properties in nanometric films with thicknesses less than the electron mean free path (typically tens of nm) [60], are strongly size dependent. For instance, thin metallic films have been reported to exhibit thickness dependent transport properties, including reduced melting points and orders of magnitude lower thermal conductivities in comparison to their bulk counterparts [59,61]. In our simulations, we consider bulk thermal conductivities and compare damage threshold temperatures to bulk melting temperatures. Lastly, we assume temperature-independent values of thin film absorption in our simulations for the sake of simplicity, but thin film absorption is generally expected to increase at higher temperatures [44,62,63]. All the above-mentioned reasons could explain the reason behind laser damage occurring below the calculated melting temperatures.

5. Outlook and conclusions

In this work, we perform a comprehensive study of laser damage performance of model nanophotonic thin films (metal, compound nitride, oxide), in relation to their optoelectrical properties for key photonic material systems. Our study is aimed towards optimizing their thermal and optical response for the design of damage resistant, functional and active nanophotonic devices for high power beam manipulation. From our experimental observations and modeling studies, we find unexpectedly that Au exhibits the best laser damage resistance among other films (TiN, TiN_xO_y and ITO) of comparable thicknesses. In general, a clear correlation exists between poorer optical FOMs, higher damping factors and degraded laser damage resistance. Further, we model the spatial thermal dissipation dynamics upon single pulse illumination, by incorporating ellipsometric dielectric permittivity values to calculate absorption (within the thin film layer) and anchoring experimentally obtained pulsed laser damage thresholds into the model. The optothermal simulations suggest that temperature rise within the thin film layer can reach temperatures corresponding to the film's bulk melting temperatures within the first nanosecond following single pulse illumination (with pulse length = 3.6 ns), confirming our claim (from morphological observation of damage spots) that laser damage in our studies is largely absorption-dominated. Thus, although TiN and TiN_xO_y compounds have been proposed as alternatives to replace noble metals due to their refractory nature (high melting points) and tunable optical properties, large absorption losses arising from high carrier concentrations and low mobilities, lead to exacerbated degradation and poorer laser damage performance at $\lambda \sim 1$ μm. However, we believe that alternative plasmonic materials and other new material platforms could prove beneficial for applications where the laser damage resistance can be traded off for tunable optical properties and CMOS compatibility, especially at lower (near- to mid-IR) frequencies [55], or for applications requiring high temperature functionality [44,62]. Improved

Optics EXPRESS

fabrication efforts in producing thin films with reduced defects and increased charge carrier mobility could also enable the integration of metal alternatives. Additionally, ITO offers a good platform to achieve optical transparency, conductivity (with large charge carrier mobilities despite high doping levels) and tunability [22,25], all with respectable laser damage performance [40]. Note that the optical and electrical properties of ITO are also strongly dependent on fabrication conditions (deposition process, oxygen content, etc.). This enables the possibility to engineer other TCOs with lower damping losses and higher thermal conductivities (to dissipate the heat more effectively). Alternatively, phase change materials such as GSTs and VO_2 can be optimized to exhibit low-loss tunabilty and superior damage performance, in combination with thermal ruggedization strategies [29,31,34,40].

In general, the laser damage performance of thin film systems can be improved by several strategies. Although the choice of a substrate has an inconsequential effect on the optical properties of optical devices (for small variations in the refractive indices), it does have a significant effect on the laser damage properties. Thus, substrates with higher thermal conductivities are desired for increasing laser damage resistance since the deposited heat can be extracted quicker. In our studies, we confirm this by comparing Au films of identical thicknesses (50 nm), deposited on sapphire and fused silica substrates. The LIDT of Au/sapphire was 2.97 J/cm^2, whereas that of Au/silica was 0.7 J/cm^2, further establishing thermally activated processes as the driver of laser damage in our study. The $\sim 4\times$ improvement in the laser damage resistance is primarily due to the difference in thermal conductivities of the two substrates. Our transient thermal distribution simulations (performed using experimentally anchored threshold fluence values) support this observation as the predicted temperature increase in Au/silica (to 793 K) occurs at a set fluence = 0.7 J/cm^2 (Supplement 1, Fig. S4). Laser damage resistance can also be improved by varying the thickness of the optical film within a device. We observed that the LIDT of 300 nm Au is $\sim$ 1.7-fold larger than that of a 50 nm Au film. This result is in line with previous predictions of a roughly linear dependence of LIDT on the thickness of absorbing films for short (ns) pulses up to 200 nm, beyond which damage was shown to be independent of film thickness [64]. However, the scaling can be drastically different in the CW and ultrafast regimes, and for non-metallic thin films, where interference effects and carrier density variations could occur [25,64]. The thicknesses of all thin film samples reported our studies were maintained between 40-70 nm, so thickness-dependent optothermal effects, if any, are expected to be minimal. It is important to note that we consider only the single-shot laser damage performance of optical thin films in our studies. For realistic applications (like metal AM), it is important to study and understand the CW and quasi-CW *lifetime* laser damage performance of a working device, where mechanisms leading to laser damage can be starkly different [65,66]. Moreover, while nanosecond pulse-induced damage threshold is in general $\propto \tau^{1/2}$, where τ is the pulse width, the scaling is expected to deviate in the limit of the thermal relaxation time for metals (ultrashort pulse regime) and conversely for CW illumination [35,67].

Nevertheless, our initial observations reported here is a first step towards future device scale studies and modeling of laser damage performance for applicability towards high power beam manipulation using nanophotonic devices. To this end, we are currently exploring the optical and thermomechanical performance of a beam steering metasurface device (optimized based on the insights gained from this current work), under passive and active (applied bias) conditions for high power CW illumination in the near-IR. However, this topic is outside the limited scope of the current work and will be the subject of future studies. Finally, our work provides insights into the management and mitigation of laser induced damage for future directions towards ruggedization and active cooling strategies for designing a broader class of functional nanophotonic materials and systems capable of high laser power operation.

Funding. U.S. Department of Energy (DE-AC52-07NA27344); Lawrence Livermore National Laboratory (19-FS-032).

Optics EXPRESS

Acknowledgments. This work was funded through a Laboratory Directed Research and Development grant 19-FS-032 and performed under the auspices of the U.S. Department of Energy by Lawrence Livermore National Laboratory under Contract DE-AC52-07NA27344. The authors would like to thank Antonio Barrios for help with sample preparation and Jae Hyuck Yoo for assistance with the laser damage setup. LLNL-JRNL-816061.

Disclosures. The authors declare no conflicts of interest.

Supplemental document. See Supplement 1 for supporting content.

References

1. R. Kirchain and L. Kimerling, "A roadmap for nanophotonics," Nat. Photonics **1**(6), 303–305 (2007).
2. N. Yu and F. Capasso, "Flat optics with designer metasurfaces," Nat. Mater. **13**(2), 139–150 (2014).
3. M. L. Brongersma, N. J. Halas, and P. Nordlander, "Plasmon-induced hot carrier science and technology," Nat. Nanotechnol. **10**(1), 25–34 (2015).
4. N. Savage, "Digital spatial light modulators," Nat. Photonics **3**(3), 170–172 (2009).
5. Y.-W. Huang, H. W. H. Lee, R. Sokhoyan, R. A. Pala, K. Thyagarajan, S. Han, D. P. Tsai, and H. A. Atwater, "Gate-Tunable Conducting Oxide Metasurfaces," Nano Lett. **16**(9), 5319–5325 (2016).
6. G. K. Shirmanesh, R. Sokhoyan, P. C. Wu, and H. A. Atwater, "Electro-optically Tunable Multifunctional Metasurfaces," ACS Nano **14**(6), 6912–6920 (2020).
7. A. M. Shaltout, V. M. Shalaev, and M. L. Brongersma, "Spatiotemporal light control with active metasurfaces," Science **364**(6441), eaat3100 (2019).
8. J. Park, J.-H. Kang, X. Liu, S. J. Maddox, K. Tang, P. C. McIntyre, S. R. Bank, and M. L. Brongersma, "Dynamic thermal emission control with InAs-based plasmonic metasurfaces," Sci. Adv. **4**(12), eaat3163 (2018).
9. T. Roy, S. Zhang, I. W. Jung, M. Troccoli, F. Capasso, and D. Lopez, "Dynamic metasurface lens based on MEMS technology," APL Photonics **3**(2), 021302 (2018).
10. I. Fomenkov, D. Brandt, A. Ershov, A. Schafgans, Y. Tao, G. Vaschenko, S. Rokitski, M. Kats, M. Vargas, M. Purvis, R. Rafac, B. La Fontaine, S. De Dea, A. LaForge, J. Stewart, S. Chang, M. Graham, D. Riggs, T. Taylor, M. Abraham, and D. Brown, "Light sources for high-volume manufacturing EUV lithography: technology, performance, and power scaling," Adv. Opt. Technol. **6**, 173 (2017).
11. H. Atikian, P. Latawiec, X. Xiong, S. Meesala, S. Gauthier, D. Wintz, J. Randi, D. Bernot, S. DeFrances, J. Thomas, M. Roman, S. Durrant, F. Capasso, and M. Loncar, "Diamond Mirror for High Power Lasers," arXiv.org 1909.06458, (2019).
12. M. J. Matthews, G. Guss, D. R. Drachenberg, J. A. Demuth, J. E. Heebner, E. B. Duoss, J. D. Kuntz, and C. M. Spadaccini, "Diode-based additive manufacturing of metals using an optically-addressable light valve," Opt. Express **25**(10), 11788–11800 (2017).
13. P. F. McManamon, P. J. Bos, M. J. Escuti, J. Heikenfeld, S. Serati, H. Xie, and E. A. Watson, "A Review of Phased Array Steering for Narrow-Band Electrooptical Systems," Proc. IEEE **97**(6), 1078–1096 (2009).
14. J. Scheuer, "Metasurfaces-based holography and beam shaping: engineering the phase profile of light," Nanophotonics **6**(1), 137–152 (2017).
15. A. Olivieri, C. Chen, S. Hassan, E. Lisicka-Skrzek, R. N. Tait, and P. Berini, "Plasmonic Nanostructured Metal–Oxide–Semiconductor Reflection Modulators," Nano Lett. **15**(4), 2304–2311 (2015).
16. J. Sautter, I. Staude, M. Decker, E. Rusak, D. N. Neshev, I. Brener, and Y. S. Kivshar, "Active Tuning of All-Dielectric Metasurfaces," ACS Nano **9**(4), 4308–4315 (2015).
17. P. C. Wu, R. A. Pala, G. Kafaie Shirmanesh, W.-H. Cheng, R. Sokhoyan, M. Grajower, M. Z. Alam, D. Lee, and H. A. Atwater, "Dynamic beam steering with all-dielectric electro-optic III–V multiple-quantum-well metasurfaces," Nat. Commun. **10**, 3654 (2019).
18. R. A. Maniyara, D. Rodrigo, R. Yu, J. Canet-Ferrer, D. S. Ghosh, R. Yongsunthon, D. E. Baker, A. Rezikyan, F. J. G. de Abajo, and V. Pruneri, "Tunable plasmons in ultrathin metal films," Nat. Photonics **13**(5), 328–333 (2019).
19. J. B. Khurgin and G. Sun, "In search of the elusive lossless metal," Appl. Phys. Lett. **96**(18), 181102 (2010).
20. J. B. Khurgin, "How to deal with the loss in plasmonics and metamaterials," Nat. Nanotechnol. **10**(1), 2–6 (2015).
21. P. Tassin, T. Koschny, M. Kafesaki, and C. M. Soukoulis, "A comparison of graphene, superconductors and metals as conductors for metamaterials and plasmonics," Nat. Photonics **6**(4), 259–264 (2012).
22. G. V. Naik, V. M. Shalaev, and A. Boltasseva, "Alternative Plasmonic Materials: Beyond Gold and Silver," Adv. Mater. **25**(24), 3264–3294 (2013).
23. E. Feigenbaum, K. Diest, and H. A. Atwater, "Unity-Order Index Change in Transparent Conducting Oxides at Visible Frequencies," Nano Lett. **10**(6), 2111–2116 (2010).
24. M. A. Noginov, L. Gu, J. Livenere, G. Zhu, A. K. Pradhan, R. Mundle, M. Bahoura, Y. A. Barnakov, and V. A. Podolskiy, "Transparent conductive oxides: Plasmonic materials for telecom wavelengths," Appl. Phys. Lett. **99**(2), 021101 (2011).
25. H. Wang, Z. Huang, D. Zhang, F. Luo, L. Huang, Y. Li, Y. Luo, W. Wang, and X. Zhao, "Thickness effect on laser-induced-damage threshold of indium-tin oxide films at 1064 nm," J. Appl. Phys. **110**(11), 113111 (2011).
26. C. M. Zgrabik and E. L. Hu, "Optimization of sputtered titanium nitride as a tunable metal for plasmonic applications," Opt. Mater. Express **5**(12), 2786 (2015).

Optics EXPRESS

27. L. Braic, N. Vasilantonakis, A. Mihai, I. J. Villar Garcia, S. Fearn, B. Zou, N. M. Alford, B. Doiron, R. F. Oulton, S. A. Maier, A. V. Zayats, and P. K. Petrov, "Titanium Oxynitride Thin Films with Tunable Double Epsilon-Near-Zero Behavior for Nanophotonic Applications," ACS Appl. Mater. Interfaces **9**(35), 29857–29862 (2017).
28. H. Liu, J. Lu, and X. R. Wang, "Metamaterials based on the phase transition of VO2," Nanotechnology **29**(2), 024002 (2018).
29. Y. Kim, P. C. Wu, R. Sokhoyan, K. Mauser, R. Glaudell, G. Kafaie Shirmanesh, and H. A. Atwater, "Phase Modulation with Electrically Tunable Vanadium Dioxide Phase-Change Metasurfaces," Nano Lett. **19**(6), 3961–3968 (2019).
30. Q. Wang, E. T. F. Rogers, B. Gholipour, C.-M. Wang, G. Yuan, J. Teng, and N. I. Zheludev, "Optically reconfigurable metasurfaces and photonic devices based on phase change materials," Nat. Photonics **10**(1), 60–65 (2016).
31. F. Ding, Y. Yang, and S. I. Bozhevolnyi, "Dynamic Metasurfaces Using Phase-Change Chalcogenides," Adv. Opt. Mater. **7**(14), 1801709 (2019).
32. R. M. Wood, *Selected Papers on Laser Damage in Optical Materials* (SPIE Optical Engineering Press, 1990).
33. S. Elhadj, J. Yoo, R. A. Negres, M. G. Menor, J. J. Adams, N. Shen, D. A. Cross, I. L. Bass, and J. D. Bude, "Optical damage performance of conductive widegap semiconductors: spatial, temporal, and lifetime modeling," Opt. Mater. Express **7**(1), 202 (2017).
34. J.-H. Yoo, A. Lange, J. Chesser, S. Falabella, and S. Elhadj, "A Survey of Transparent Conducting Films and Optoelectrical Materials for High Optical Power Applications," Phys. Status Solidi A **216**(22), 1900459 (2019).
35. D. Ristau, M. Jupé, and K. Starke, "Laser damage thresholds of optical coatings," Thin Solid Films **518**(5), 1607–1613 (2009).
36. J.-Y. Natoli, L. Gallais, H. Akhouayri, and C. Amra, "Laser-induced damage of materials in bulk, thin-film, and liquid forms," Appl. Opt. **41**(16), 3156 (2002).
37. P. E. Nielsen, *Effects of Directed Energy Weapons: Lasers, High Power Microwaves, Particle Beams* by Philip E. Nielsen, (Directed Energy Professional Society, 1994).
38. S. K. Saha, D. Wang, V. H. Nguyen, Y. Chang, J. S. Oakdale, and S.-C. Chen, "Scalable submicrometer additive manufacturing," Science **366**(6461), 105–109 (2019).
39. D. Heath, "Digital micromirror devices and femtosecond laser pulses for rapid laser micromachining," Doctoral dissertation, University of Southampton (2017).
40. J.-H. Yoo, M. Matthews, P. Ramsey, A. C. Barrios, A. Carter, A. Lange, J. Bude, and S. Elhadj, "Thermally ruggedized ITO transparent electrode films for high power optoelectronics," Opt. Express **25**(21), 25533 (2017).
41. W. Li, U. Guler, N. Kinsey, G. V. Naik, A. Boltasseva, J. Guan, V. M. Shalaev, and A. V. Kildishev, "Refractory Plasmonics with Titanium Nitride: Broadband Metamaterial Absorber," Adv. Mater. **26**(47), 7959–7965 (2014).
42. L. Gui, S. Bagheri, N. Strohfeldt, M. Hentschel, C. M. Zgrabik, B. Metzger, H. Linnenbank, E. L. Hu, and H. Giessen, "Nonlinear Refractory Plasmonics with Titanium Nitride Nanoantennas," Nano Lett. **16**(9), 5708–5713 (2016).
43. B. T. Diroll, S. Saha, V. M. Shalaev, A. Boltasseva, and R. D. Schaller, "Broadband Ultrafast Dynamics of Refractory Metals: TiN and ZrN," Adv. Opt. Mater. **8**(19), 2000652 (2020).
44. H. Reddy, U. Guler, Z. Kudyshev, A. V. Kildishev, V. M. Shalaev, and A. Boltasseva, "Temperature-Dependent Optical Properties of Plasmonic Titanium Nitride Thin Films," ACS Photonics **4**(6), 1413–1420 (2017).
45. M. P. Wells, R. Bower, R. Kilmurray, B. Zou, A. P. Mihai, G. Gobalakrichenane, N. M. Alford, R. F. M. Oulton, L. F. Cohen, S. A. Maier, A. V. Zayats, and P. K. Petrov, "Temperature stability of thin film refractory plasmonic materials," Opt. Express **26**(12), 15726 (2018).
46. M. Born and E. Wolf, *Principles of Optics: Electromagnetic Theory of Propagation, Interference and Diffraction of Light* (Cambridge University, 1999).
47. T. Ashida, A. Miyamura, N. Oka, Y. Sato, T. Yagi, N. Taketoshi, T. Baba, and Y. Shigesato, "Thermal transport properties of polycrystalline tin-doped indium oxide films," J. Appl. Phys. **105**(7), 073709 (2009).
48. V. Linseis, F. Völklein, H. Reith, K. Nielsch, and P. Woias, "Thermoelectric properties of Au and Ti nanofilms, characterized with a novel measurement platform," Mater. Today: Proc. **8**, 517–522 (2019).
49. Y. Jee, M. F. Becker, and R. M. Walser, "Laser-induced damage on single-crystal metal surfaces," J. Opt. Soc. Am. B **5**(3), 648 (1988).
50. W.-P. Guo, R. Mishra, C.-W. Cheng, B.-H. Wu, L.-J. Chen, M.-T. Lin, and S. Gwo, "Titanium Nitride Epitaxial Films as a Plasmonic Material Platform: Alternative to Gold," ACS Photonics **6**(8), 1848–1854 (2019).
51. C.-C. Chang, J. Nogan, Z.-P. Yang, W. J. M. Kort-Kamp, W. Ross, T. S. Luk, D. A. R. Dalvit, A. K. Azad, and H.-T. Chen, "Highly Plasmonic Titanium Nitride by Room-Temperature Sputtering," Sci. Rep. **9**(1), 15287 (2019).
52. R. P. Sugavaneshwar, S. Ishii, T. D. Dao, A. Ohi, T. Nabatame, and T. Nagao, "Fabrication of Highly Metallic TiN Films by Pulsed Laser Deposition Method for Plasmonic Applications," ACS Photonics **5**(3), 814–819 (2018).
53. O. Tuna, Y. Selamet, G. Aygun, and L. Ozyuzer, "High quality ITO thin films grown by dc and RF sputtering without oxygen," J. Phys. D: Appl. Phys. **43**(5), 055402 (2010).
54. A. P. Amalathas and M. M. Alkaisi, "Effects of film thickness and sputtering power on properties of ITO thin films deposited by RF magnetron sputtering without oxygen," J. Mater. Sci.: Mater. Electron. **27**(10), 11064–11071 (2016).
55. J. B. Khurgin and A. Boltasseva, "Reflecting upon the losses in plasmonics and metamaterials," MRS Bull. **37**(8), 768–779 (2012).
56. D. I. Yakubovsky, A. V. Arsenin, Y. V. Stebunov, D. Y. Fedyanin, and V. S. Volkov, "Optical constants and structural properties of thin gold films," Opt. Express **25**(21), 25574 (2017).
57. G. Baffou, "Mapping Heat Origin in Plasmonic Structures," Phys. Rev. Lett. **104**(13), 136805 (2010).

Optics EXPRESS

58. Q. Jiang, S. Zhang, and M. Zhao, "Size-dependent melting point of noble metals," Mater. Chem. Phys. **82**(1), 225–227 (2003).
59. S. J. Henley, "Pulsed-laser-induced nanoscale island formation in thin metal-on-oxide films," Phys. Rev. B **72**(19), 195408 (2005).
60. E. H. Sondheimer, "The mean free path of electrons in metals," Adv. Phys. **1**(1), 1–42 (1952).
61. A. H. Guenther and J. K. Mciver, "The role of thermal conductivity in the pulsed laser damage sensitivity of optical thin films," Thin Solid Films **163**, 203–214 (1988).
62. J. A. Briggs, G. V. Naik, Y. Zhao, T. A. Petach, K. Sahasrabuddhe, D. Goldhaber-Gordon, N. A. Melosh, and J. A. Dionne, "Temperature-dependent optical properties of titanium nitride," Appl. Phys. Lett. **110**(10), 101901 (2017).
63. H. Reddy, U. Guler, A. V. Kildishev, A. Boltasseva, and V. M. Shalaev, "Temperature-dependent optical properties of gold thin films," Opt. Mater. Express **6**(9), 2776 (2016).
64. B. C. Stuart, M. D. Feit, S. Herman, A. M. Rubenchik, B. W. Shore, and M. D. Perry, "Optical ablation by high-power short-pulse lasers," J. Opt. Soc. Am. B **13**(2), 459 (1996).
65. X. Liu, L. Peng, Y. Gao, Y. Zhao, Y. Liu, D. Li, M. Zhu, Z. Cao, J. Shao, and X. Wang, "Laser damage characteristics of indium-tin-oxide film and polyimide film," Infrared Phys. Technol. **99**, 80–85 (2019).
66. L. Peng, Y. Zhao, X. Liu, Z. Cao, D. Li, Y. Lian, H. Ma, R. Hong, C. Tao, D. Zhang, and J. Shao, "Temperature dependence of initial deformation and cracks of indium tin oxide film by quasi-continuous-wave laser irradiations," Opt. Mater. Express **10**(10), 2394–2405 (2020).
67. B. C. Stuart, "Laser-Induced Damage in Dielectrics with Nanosecond to Subpicosecond Pulses," Phys. Rev. Lett. **74**(12), 2248–2251 (1995).